



Terahertz topological plasmon polaritons for robust temperature sensing

B. X. Wang  and C. Y. Zhao *

Institute of Engineering Thermophysics, School of Mechanical Engineering, Shanghai Jiao Tong University, Shanghai 200240, China
MOE Key Laboratory for Power Machinery and Engineering, Shanghai Jiao Tong University, Shanghai 200240, China



(Received 13 November 2019; accepted 23 June 2020; published 13 July 2020)

We theoretically investigate the application of topological plasmon polaritons (TPPs) to achieving robust temperature sensing. Based on an analogy of the topological edge states in the Su-Schrieffer-Heeger model, TPPs are realized in a one-dimensional intrinsic indium antimonide (InSb) microsphere chain. The existence of TPPs is demonstrated by analyzing the topology of the photonic band structures and the eigenmode distribution. Due to the temperature dependence of the permittivity of InSb in the terahertz range, the resonance frequency of TPPs can be largely tuned by the temperature. The temperature susceptibility of the TPP resonance frequency can be as high as 0.0264 THz/K at room temperature, leading to a figure of merit over 150. Based on calculations on the optical local density of states (LDOS) near the chain, it is shown that the temperature susceptibility of TPPs is experimentally detectable via near-field probing techniques. Numerical results also indicate the sensing performance is immune to disorder. We further propose a robust and practical calibration method to correctly obtain the peak frequency of the LDOS spectrum due to the TPPs and then the temperature susceptibility, which is based on the ratio between the LDOS of a topological chain and that of a nontopological one. These TPPs can be potential candidates for robust temperature sensing, for which several experimental considerations are further discussed.

DOI: [10.1103/PhysRevMaterials.4.075201](https://doi.org/10.1103/PhysRevMaterials.4.075201)

I. INTRODUCTION

Topological phases of matter can support robust edge states immune against scattering from disorder and imperfections, which have received a great deal of attention in recent years and been demonstrated for electronic [1], electromagnetic [2], acoustic [3], cold atomic [4], and mechanical [5] systems. In particular, since topological photonic systems can hold topologically protected optical modes [6–9], they provide great opportunities for achieving precise, robust, and local control of light, which facilitate high-performance photonic devices such as unidirectional waveguides [10], optical isolators [11], and topological lasers [12–14].

Notably, as a unique combination of topological protection and strong light confinement due to plasmonic excitations, topological plasmon polaritons (TPPs) are arguably among the most promising approaches to robust and deep-subwavelength scale light-matter interactions and have therefore attracted growing attention in the last a few years [15–20]. For instance, the modal wavelength of topologically bounded plasmonic modes in multilayered graphene systems can be squeezed as small as 1/70 of the incident wavelength [21]. Low-power-consumption and highly integrated four-wave mixing processes can also be engineered through the TPP modes in graphene metasurfaces [22]. As a result, the topological protection of the spectral and spatial position of TPPs with enhanced light-matter interactions indeed provides

a promising route to robust sensing, like what has been done in non-Hermitian photonics using exceptional points [23–28]. However, there have been very few works concerning topological plasmon polariton modes for sensing applications so far.

In this work, we theoretically explore the possibility of the application of TPPs to temperature sensing. Based on a photonic extension of the Su-Schrieffer-Heeger (SSH) model [29], we realize TPPs in one-dimensional (1D) dimerized indium antimonide (InSb) microsphere chains in the terahertz (THz) range, protected by the band topology that is characterized by the quantized complex Zak phase. The choice of intrinsic InSb is motivated by its temperature-dependent carrier concentration that can result in a thermally tunable plasma frequency in the THz range [30–32]. This work is also motivated by the rapid development of terahertz technologies, which makes the flexible generation [33], manipulation [34], and detection [35] of THz radiation possible and efficient, leading to promising applications in radar [36], communication [37], biological imaging [38], and microscopy [39,40]. Here, we reveal that the resonance frequency of the TPPs in the dimerized microsphere chain can be successfully tuned by the temperature, leading to a high sensitivity and figure of merit. By calculating the local density of states (LDOS) at different temperatures, we further demonstrate that this temperature sensitivity can be experimentally detected and find that the LDOS signals of these TPPs are immune to disorder, giving rise to a robust temperature sensing functionality. Furthermore, we propose that the peak frequency of the ratio between the LDOS of a topological chain and that of a nontopological one can be utilized to achieve an improved sensing performance in practice.

*changying.zhao@sjtu.edu.cn

II. MODEL

In Fig. 1(a), the 1D InSb microspheres chain is assumed to be aligned along the x -axis, where the dimerization is introduced by using inequivalent spacings d_1 and d_2 for the two sublattices, denoted by A and B with a dimerization parameter defined as $\beta = d_1/d$ where $d = d_1 + d_2$ is the lattice constant. This dimerization process gives rise to different “hopping” amplitudes of plasmon polaritons in either directions, well mimicking the SSH model for electrons [29]. Note due to the presence of near-field and far-field dipole-dipole interactions, a theoretical model beyond the nearest-neighbor approximation in the conventional SSH model should be implemented [41,42]. To this end, the radius of the InSb microsphere is set to be $a = 1 \mu\text{m}$, which is much smaller than the wavelength of interest (usually larger than $100 \mu\text{m}$). The electromagnetic response of an individual InSb microsphere is then described by the electric dipole polarizability with the radiative correction given by

$$\alpha(\omega) = \frac{4\pi a^3 \alpha_0}{1 - 2i\alpha_0(ka)^3/3}, \quad (1)$$

where $\alpha_0(\omega) = \frac{\varepsilon_p(\omega)-1}{\varepsilon_p(\omega)+2}$, ω is the angular frequency of the driving field and $k = \omega/c$ is the wave number with c denoting the speed of light in vacuum [43–45]. The permittivity function

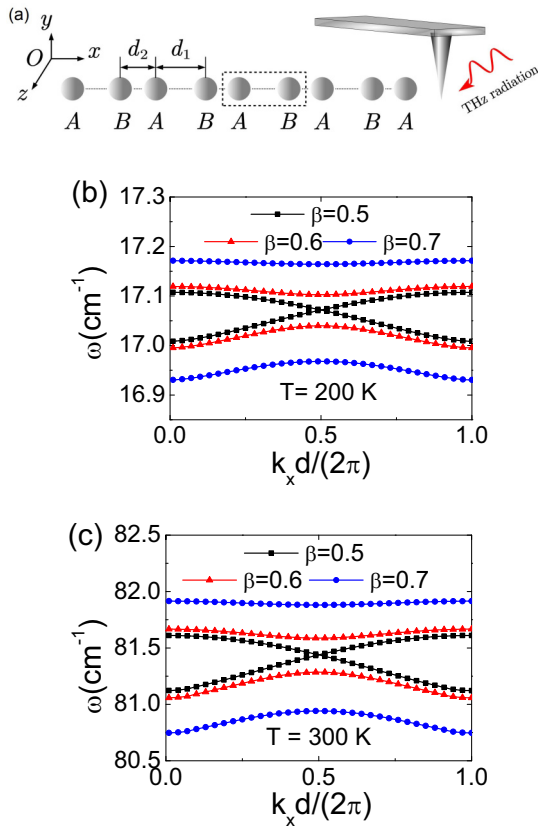


FIG. 1. (a) Schematic of the dimerized InSb microsphere chain with a scattering-type SNOM tip nearby and THz incident radiation. (b)–(c) Real parts of the longitudinal band structures of a dimerized InSb microsphere chain under a temperature of (b) 200 and (c) 300 K with different β .

of intrinsic InSb can be modeled by a Drude model as

$$\varepsilon_p(\omega) = \varepsilon_\infty - \frac{\omega_p^2}{\omega^2 + i\gamma\omega}, \quad (2)$$

where $\varepsilon_\infty = 15.68$ is the high-frequency limit of the permittivity, ω_p is the plasma frequency, and γ is the damping coefficient, both of which depend on the temperature [30,46,47]. In particular, $\omega_p = \sqrt{N_c e^2 / m^* \varepsilon_0}$ and $\gamma = e / m^* \mu$, where N_c is the carrier concentration, m^* is the effective mass of carries, μ is the mobility, e is the electric charge of an electron, and ε_0 is the permittivity of the vacuum.

In the investigated temperature range in this work, the carrier mobility varies very slightly with the temperature and thus can be regarded as constant [46,48], leading to a decay rate of $\gamma = 10\pi \times 10^{10} \text{ rad/s}$ [30,48]. The effective mass is chosen to be $m^* = 0.015m_e$ [49]. When the temperature T is in the range from 160 to 350 K, the energy gap of InSb changes very little, and its the carrier concentration N_c (in cm^{-3}) as a function of temperature is described by the following experimental correlation equation [30,46,47,50]:

$$N_c = 5.76 \times 10^{14} T^{\frac{3}{2}} \exp\left(-\frac{0.13\text{eV}}{k_B T}\right), \quad (3)$$

where k_B is the Boltzmann constant. When the distance between the centers of different microspheres is larger than $3a$, higher multipolar excitations can be neglected, and thus the electromagnetic interactions are adequately described by following coupled-dipole equations [43–45]:

$$\mathbf{p}_j(\omega) = \alpha(\omega) \left[\mathbf{E}_{\text{inc}}(\mathbf{r}_j) + \frac{\omega^2}{c^2} \sum_{i=1, i \neq j}^{\infty} \mathbf{G}_0(\omega, \mathbf{r}_j, \mathbf{r}_i) \mathbf{p}_i(\omega) \right], \quad (4)$$

where $\mathbf{E}_{\text{inc}}(\mathbf{r})$ is the external incident field and $\mathbf{p}_j(\omega)$ is the excited electric dipole moment of the j th microsphere. $\mathbf{G}_0(\omega, \mathbf{r}_j, \mathbf{r}_i)$ is the free-space dyadic Green’s function describing the propagation of field emitting from the i th microsphere to j th microsphere [44], which is given by

$$\mathbf{G}_0(\mathbf{r}_j, \mathbf{r}_i) = \frac{\exp(ikr)}{4\pi r} \left(\frac{i}{kr} - \frac{1}{k^2 r^2} + 1 \right) \mathbf{I} + \frac{\exp(ikr)}{4\pi r} \left(-\frac{3i}{kr} + \frac{3}{k^2 r^2} - 1 \right) \hat{\mathbf{r}}\hat{\mathbf{r}} - \frac{\delta(\mathbf{r})}{3k^2}, \quad (5)$$

where $k = \omega/c$ is the free-space wave number. The Dirac delta function $\delta(\mathbf{r})$ is responsible for the so-called local field in the scatterers [51]. This model takes all types of near-field and far-field dipole-dipole interactions into account and is thus beyond the traditional nearest-neighbor approximation [15].

III. BAND STRUCTURE AND TOPOLOGICAL MODES

According to the polarization direction of the dipole moments, the eigenmodes can be divided into two types: transverse and longitudinal [52]. More specifically, the dipole moments in the longitudinal modes are polarized along the x -axis, while those in the transverse modes are polarized

perpendicular to the x -axis. In this work, we are mainly concerned with the topological properties of longitudinal modes. This is because transverse ones are more strongly coupled to the free-space radiation with a much narrower band gap and the localization degree is lower due to the long-range dipole-dipole interactions, all of which make it difficult to observe transverse topological eigenmodes experimentally, as discussed in our previous papers [41,42]. We will also see that in Fig. 4, the near-field detected signal is mainly determined by the longitudinal modes [42].

To identify the topological properties, we first calculate the longitudinally polarized band structures. The calculation is done by applying the Bloch theorem to Eq. (4) for an infinitely long chain, which results in the following two-band dispersion relation [41,42]:

$$\frac{1}{4\pi(ka)^3} \frac{\varepsilon_p(\omega) + 2}{\varepsilon_p(\omega) - 1} - \frac{i}{6\pi} = a_{11}^L(k_x) \pm \sqrt{a_{12}^L(k_x) a_{21}^L(k_x)}, \quad (6)$$

where $a_{11}^L(k_x)$, $a_{12}^L(k_x)$, $a_{21}^L(k_x)$ are the matrix elements of the effective ‘‘Hamiltonian’’ of the system with expressions presented in Appendix A. By sweeping the Bloch wave vector (momentum) k_x across the first Brillouin zone and solving the eigenfrequencies from Eq. (6) in the lower complex plane, we can immediately obtain the band structure. The solved eigenfrequencies are generally expressed in the complex form of $\tilde{\omega} = \omega - i\Gamma/2$ indicating the non-Hermitian property of the present system [42], where the real part ω amounts to the angular frequency while the imaginary part Γ corresponds to the linewidth (or decay rate) of the eigenmode [17]. Note in the above equation, the radius a only affects the detailed values of the eigenfrequencies, as long as the electric dipole approximation with the radiative correction and coupled-dipole model are valid, not having any qualitative impact on the band topology [42]. Therefore, without loss of generality, we adopt a fixed radius throughout the paper.

In Figs. 1(b) and 1(c), the real parts of the longitudinal band structures under two different temperatures of $T = 200$ and 300 K are presented, respectively, for different dimerization parameters at a fixed lattice constant of $d = 10 \mu\text{m}$. Since band structures are identical for the cases of β and $1 - \beta$ with the difference lying in their topological invariant [16,17], the band structures for the cases of $\beta = 0.3$ and $\beta = 0.4$ are not plotted. For $\beta \neq 0.5$, band gaps in the real frequency space persist to be open and a larger $|\beta - 0.5|$ gives rise to a wider band gap. This behavior is consistent with the conventional SSH model [4]. Moreover, at different temperatures, the central frequency of the band gap is vastly different, actually close to the frequency of the localized surface plasmon resonance (LSPR) of a single microsphere at different temperatures, as a result of the strong coupling between the collective, delocalized surface plasmon polariton (SPP) modes of the two sublattices at $\beta \neq 0.5$ [42].

While the present system is open and hence non-Hermitian, for longitudinal modes the non-Hermiticity in essence does not break the bulk-boundary correspondence (BBC) and the complex Zak phase θ_Z is adequate to capture the topological properties in the bulk side, which is the geometric phase

picked up by an eigenmode when it adiabatically evolves across the first Brillouin zone (BZ), as proven by previous works [41,42,53], from which as well as Appendix B more details can be found. Moreover, although in the present system the chiral symmetry breaks down, θ_Z is still quantized (having only two values, 0 and π) in a similar way as in the chirally symmetric system because the eigenvectors are independent of the chiral-symmetry breaking terms in the effective Hamiltonian [17,41,42]. Calculation shows that the complex Zak phase for $\beta = 0.7$ and $\beta = 0.6$ is π and 0 for $\beta = 0.3$ and $\beta = 0.4$. Detailed calculation and relevant discussions on the complex Zak phase are also presented in Appendix B. Furthermore, we examined that regardless of the lattice constant and temperature, the complex Zak phase is guaranteed to be 0 for $\beta < 0.5$ and π for $\beta > 0.5$ for longitudinal modes [41,42]. Consequently in the present system, the complex Zak phase is a well-defined topological invariant in the bulk side, which can be summarized using the following expression:

$$\theta_Z = \begin{cases} \pi & \beta > 0.5, & (1 - \beta)d \geq 3a, \\ 0 & \beta < 0.5, & \beta d \geq 3a, \end{cases} \quad (7)$$

where the restrictions on the geometric parameters (β and a) are made solely as a requirement of the validity of the dipole approximation.

To examine the bulk-boundary correspondence (BBC), a crucial principle in topological physics, we then turn to a finite system under the open boundary condition and calculate its eigenmode distribution (i.e., discrete band structures). This can be done by using Eq. (4) with a zero incident field [17,52]. More specifically, an eigenvalue equation in the form of $\mathbf{G}|\mathbf{p}\rangle = \alpha^{-1}(\omega)|\mathbf{p}\rangle$ is obtained, with \mathbf{G} standing for the interaction Green’s matrix and $|\mathbf{p}\rangle = [p_1 p_2 \dots p_j \dots p_N]$ denoting the right eigenvector or the dipole moment distribution of an eigenmode with p_j the dipole moment of the j th microsphere. This equation also gives rise to a discrete set of complex eigenfrequencies in the lower complex plane for the eigenmodes [17,41,42]. Additionally, for each eigenmode, the inverse participation ratio (IPR) is calculated to quantify its degree of spatial localization

$$\text{IPR} = \frac{\sum_{n=1}^N |p_j|^4}{\left(\sum_{n=1}^N |p_j|^2\right)^2}, \quad (8)$$

which is closer to 1 for a more spatially localized eigenmode [41,54]. The eigenmode spectra for the cases of $\beta = 0.7$ [Fig. 2(a)] and $\beta = 0.3$ [Fig. 2(b)] under $T = 300$ K are presented. In both cases complex band gaps keep open, consistent with the complex band gaps in the Bloch band structure. However, a significant difference between the $\beta = 0.7$ and $\beta = 0.3$ cases can be noted, which is that there are two midgap modes with high IPRs in the band gap in the former case. The dipole moment distributions of the two midgap modes are shown in the inset of Fig. 2(a), which are found to be highly localized over both boundaries and thus have large IPRs reaching 0.5 (namely, mainly localized over two microspheres). By considering the nontrivial complex Zak phase of the $\beta = 0.7$ case in the bulk side, it can be verified that these midgap modes are topologically protected edge modes, namely, topological plasmon polaritons [25,55].

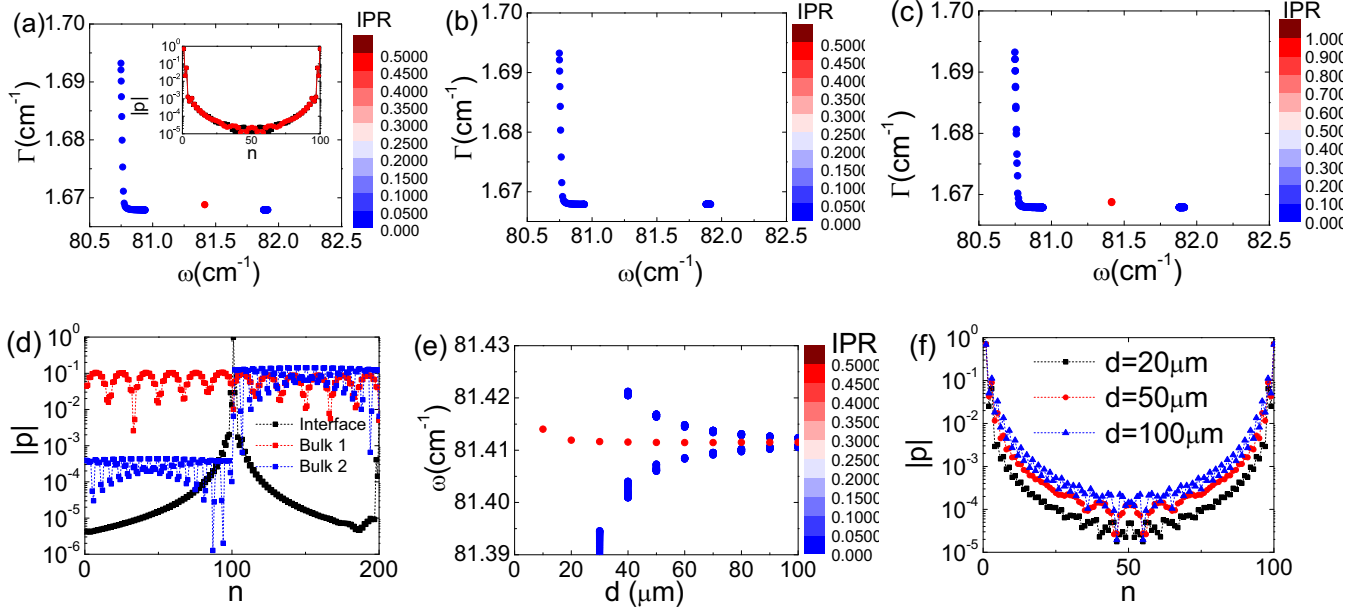


FIG. 2. Topological eigenmodes in finite systems at $T = 300$ K. (a) Longitudinal eigenmode distribution of a dimerized chain with $N = 100$ microspheres under $\beta = 0.7$ and $d = 10 \mu\text{m}$. Note there are two spectrally overlapping midgap modes. Inset: Dipole moment distribution of the midgap edge modes. (b) The same as (a) but here $\beta = 0.3$. (c) Longitudinal eigenmode distribution for a connected chain. (d) Dipole moment distribution of the interface mode in (c), compared to those of two arbitrarily chosen bulk eigenmodes. (e) Real parts of the complex eigenfrequency spectrum of longitudinal eigenmodes as a function of the lattice constant d for $\beta = 0.7$. (f) Dipole moment distribution for the topological edge modes at different lattice constants.

To further demonstrate the BBC, Fig. 2(c) shows the eigenmode distribution of a 1D connected chain consisting of a topologically trivial chain with $\beta = 0.3$ in the left and a topologically nontrivial chain with $\beta = 0.7$ in the right. The distance between the two chains is set to be $10 \mu\text{m}$. We can clearly observe two midgap modes with high IPRs reaching over 0.9 (namely, mainly localized over one microsphere), one of which is the topological interface mode while the other is the topological edge mode localized at the right boundary of the right chain. In addition, in Fig. 2(d), the dipole moment distribution for the topological interface mode is shown compared to those of two typical bulk eigenmodes, which are extended over the chain. To investigate the effect of lattice constant on the topological edge modes, the real part of the eigenfrequency spectrum of a finite chain as a function of the lattice constant is presented in Fig. 2(e) with the dimerization parameter fixed as $\beta = 0.7$. It is found that the complex band gaps persist to be open with high-IPR eigenmodes robustly emerging in the complex band gaps. Note at large lattice constants, the real band gap almost closes while the imaginary part still opens, which are not shown here for brevity. In addition, the complex frequency of the topological modes hardly varies with the increase of the lattice constant, indicating its robustness (with a variation of angular frequency smaller than 0.003 cm^{-1} or about 5 nm). The dipole moment distributions of the topological midgap modes under different lattice constants are also presented in Fig. 2(f). In addition, we also confirm that for the cases of $\beta < 0.5$ at different lattice constants, no localized edge eigenmodes can be found. Therefore, by summarizing the results presented in Figs. 1 and 2, we can unambiguously

confirm that highly localized TPPs are found in the present system, which are topologically protected by the well-defined complex Zak phase if the dimerization parameter $\beta > 0.5$, regardless of the lattice constant and temperature.

Let us remark that the main features of our system presented in this section, including the band structures, the definition and quantization of the complex Zak phase, the emergence of topological edge modes and the validity of the BBC, are in line with the general properties of 1D dimerized dipolar chains, which have been thoroughly studied in previous works under different physical settings [15–20,41,42]. The only distinction in the present work is that the TPPs exist in the THz range and can be tuned by the temperature due to the intrinsic property of the InSb material. More details on the general properties of 1D dimerized dipolar chains can be found in aforementioned works and Appendixes A and B.

IV. TEMPERATURE SENSING APPLICATION

In this section, we investigate the effects of temperature on these TPPs and their application to temperature sensing. In Fig. 3, we show the variation of resonance frequencies of edge and interface TPPs with the temperature. It is observed that the resonance frequency of TPPs can be varied in a wide frequency range from about 0.2 to 4 THz by increasing the temperature from 160 to 350 K. The frequencies of edge and interface TPPs almost overlap with each other, indicating the spectral stability of these topological modes against geometric parameters. The band gaps also become wider as the temperature grows, which makes it easier for experimental observation of TPPs at relatively high

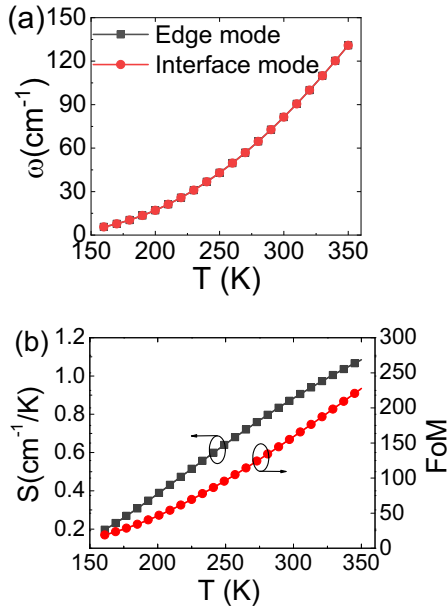


FIG. 3. (a) Effects of temperature on the resonance frequency (wavelength) of edge and interface modes of the topological plasmon polaritons. (b) Susceptibility and figure of merit (FoM) quantifying the temperature sensing performance of the topological plasmon polaritons. Here the parameters are $\beta = 0.7$ and $d = 10 \mu\text{m}$. The disordered realizations are randomly chosen.

temperatures (not shown here for brevity). These observations feature a temperature sensing functionality for the TPPs. The temperature sensing performance can be quantified by using the temperature susceptibility of the resonance frequency of TPPs, which is defined as $S = \Delta\omega_{\text{TPP}}/\Delta T$, where Δ indicates a small variation for a physical quantity [56,57]. At room temperature (approximately taken as 300 K), the susceptibility is about $0.88 \text{ cm}^{-1}/\text{K}$, or $0.0264 \text{ THz}/\text{K}$, which is equivalent to a wavelength shift around $1.3423 \mu\text{m}/\text{K}$. Moreover, we can define a figure of merit (FoM) of this temperature sensing performance as $\text{FoM} = ST/\Gamma = \Delta\omega_{\text{TPP}}T/(\Gamma\Delta T)$, which reaches over 150 at room temperature. In Fig. 3(b), the variations of S and FoM with the temperature are presented. As a comparison, a recent design of optical temperature sensors exhibited a temperature susceptibility about $8.9 \times 10^{-3} \text{ THz}/\text{K}$ and FoM around 119 [58], which are significantly lower.

In experiment, it has been shown that TPPs, or more generally, topological photonic modes, can be conveniently detected by the scanning near-field optical microscopy (SNOM) [59–61] or other high-momentum sources [62]. In THz wavelengths, scattering-type SNOM (s-SNOM) is most widely used to reach subdiffraction limited resolution [40,63–69]. The images taken by a s-SNOM can closely follow the local density of states (LDOS) distribution in the system, yet not rigorously equivalent, as demonstrated theoretically and experimentally by a number of studies [55,64,70–76]. In particular, it has been shown by recent theoretical and experimental results that the LDOS value can be deduced from the phase spectrum [77,78]. Here for simplicity, we only calculate the LDOS ρ by putting an ideal electric dipole near the chain with a distance of 100 nm at different temperatures

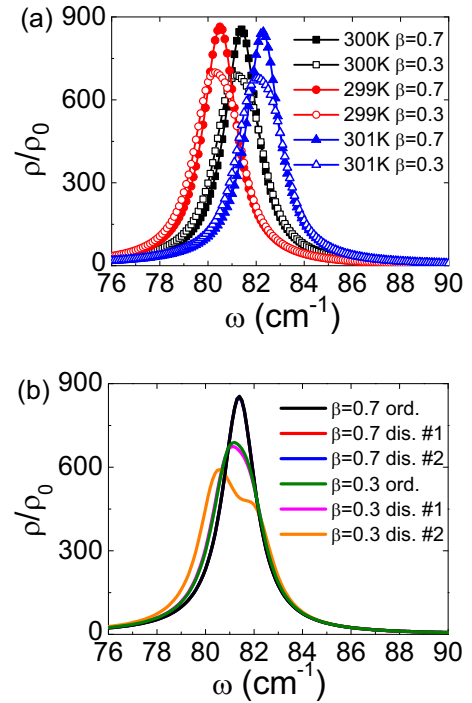


FIG. 4. Calculated LDOS as an experimentally accessible signal of TPP temperature susceptibility. (a) The LDOS values for topological and nontopological chains at different temperatures. (b) The LDOS for topological and nontopological disordered (dis.) chains at $T = 300 \text{ K}$, compared to those of ordered (ord.) ones.

as a proof-of-concept demonstration for future experiments, as schematically shown in Fig. 1(a) with a SNOM cantilever nearby. The calculation details can be found in Appendix C. The LDOS can be regarded as an indicator of the strength of light-matter interactions.

The spectra of normalized LDOS ρ/ρ_0 for both topologically nontrivial and trivial systems are summarized in Fig. 4(a), where $\rho_0 = \omega^2/(\pi^2c^3)$ is the LDOS in vacuum. For topological chains ($\beta = 0.7$), it is found that the LDOS is substantially enhanced at the center of band gaps due to the existence of TPPs. In the meanwhile, for topologically trivial chains ($\beta = 0.3$), the values of LDOS are substantially suppressed within the band gaps, and the LDOS peaks emerge at the band edges due to non-topological plasmon polaritons. As a result, there is a slight frequency shift between the LDOS peaks of topological trivial and nontrivial cases [42]. To be more specific, for $T = 300 \text{ K}$ at the resonance frequency of the TPP, namely, $\omega = 81.4 \text{ cm}^{-1}$, $\rho/\rho_0 = 854.87$ reaches its maximum for the topological chain, while the LDOS near the nontopological chain is $\rho/\rho_0 = 676.86$ at this frequency, whose peak lies at around $\omega = 81.2 \text{ cm}^{-1}$. Moreover, by slightly varying the temperature to 299 and 301 K, we can observe considerable shifts of LDOS peaks for both topological and nontopological cases.

It seems that both topological and nontopological plasmon polaritons can be used to perform temperature sensing according to Fig. 4(a). However, we will show below that the LDOS peaks due to TPPs are robust over disorder, while nontopological plasmon polaritons are severely affected by the disorder.

The disorder is introduced by shifting the positions of *B*-type microspheres randomly in the range $[-\eta d_1/2, \eta d_1/2]$ along the *x*-axis, while the positions of *A*-type microspheres are fixed, to make the lattice period *d* constant. Here η stands for the degree of disorder. Such disorder breaks both inversion and chiral symmetries, at least one of which are regarded as protecting the topological properties of the present system [17,19,42,53] (see Appendix B). In Fig. 4(b), results of the LDOS at $T = 300$ K of two randomly chosen disordered realizations under a substantial degree of disorder ($\eta = 0.3$) for both topological and non-topological chains are presented, compared with those of ordered ones. It is clearly seen that the LDOS peaks in topological chains are very robust against disorder while those of non-topological chains significantly vary with the detailed positions of microspheres. As a result, we can confirm that the temperature susceptibility of TPPs is experimentally detectable via near-field probing techniques like terahertz s-SNOM and quantum emitters [79], and the robustness of TPPs makes them advantageous over non-topological plasmon polaritons.

For s-SNOM measurements, one cannot compare the raw data obtained at different frequencies directly and quantitatively since the power of radiation sources, the incident energy upon the near-field probe, and the collection efficiency of the detection system vary from frequency to frequency, difficult to exactly determine [40,78,80]. The modulations over the probe as well as the material and geometry of the probe also play an important role in the measured signal [81]. In this circumstance, a calibration procedure based on a reference signal is usually necessary to demonstrate the characteristic spectral features solely due to the sample of interest. Conventionally, reference signals can be obtained from some spectrally featureless materials like gold or silicon [40,55,66,67,80,82–85]. However, chances are the calibration using standard references may not lead to pronounced signals of spectroscopic resonance peaks. For instance, if the LDOS measured (manifest as phase spectrum in s-SNOM) from standard reference samples is also very large, the measured peak LDOS due to TPP might be smeared. To this end, here based on the unique features of LDOS spectra of topological and nontopological chains, we propose a more robust and practical calibration method to correctly obtain the peak frequency of the LDOS spectrum due to the excitation of TPPs and thus the temperature susceptibility, which can provide more pronounced experimental indicators of the resonance frequency of TPPs. This method is also expected to reduce other experimental uncertainties.

In a topological chain the LDOS values near the microspheres inside the bulk of chain are substantially suppressed owing to the band gap, as can be seen in the top panel of Fig. 5(a), which shows a scanning LDOS map probed at a distance of 100 nm above the microsphere chains at $T = 300$ K and $\omega = 81.4$ cm⁻¹. It is observed that the LDOS values near the edge microsphere are substantially larger than those near the bulk spheres. There is no such difference in a topologically trivial chain as illustrated in the bottom panel of Fig. 5(a). Hence we can measure the ratio between the LDOS near the edge microsphere and that near other bulk microspheres, as a calibrated quantity that enables a quantitative analysis at different frequencies to determine the resonance

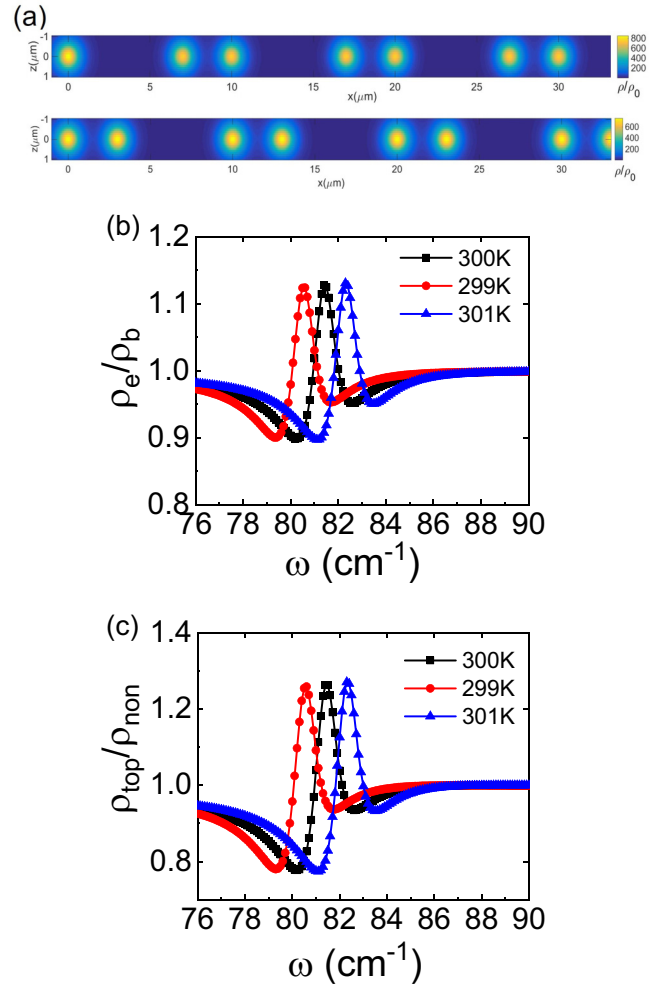


FIG. 5. Comparison of LDOS values at different situations. (a) The LDOS maps for topological (top) and nontopological (bottom) chains at $T = 300$ K and $\omega = 81.4$ cm⁻¹. The near-field probe (electric point dipole) is kept at a distance of 100 nm above the chains. (b) The ratio between the LDOS values at edge and bulk positions, ρ_e/ρ_b , for a topological chain under different temperatures. (c) The ratio between the LDOS values at the edges of topological and nontopological chains, $\rho_{\text{top}}/\rho_{\text{non}}$, under different temperatures.

peak frequency due to TPPs. We calculate this ratio ρ_e/ρ_b for the topological chain ($\beta = 0.7$) at different temperatures as shown in Fig. 5(b). It is clearly seen that the peak frequency of this ratio corresponds to the resonant frequency of TPPs. We can also confirm the peak frequency of ρ_e/ρ_b is robust against disorder [see Fig. 6(a) in Appendix C which shows the results under 100 random disordered configurations]. In addition, one can also measure the ratio between the LDOS values near the edges of topological and nontopological chains, if the two chains are fabricated in the same sample. The results of this ratio, represented by $\rho_{\text{top}}/\rho_{\text{non}}$, are provided in Fig. 5(c). It is found that this ratio exhibits more pronounced peaks than ρ_e/ρ_b , thus leading to better signals than ρ_e/ρ_b . The peak frequency of this ratio is also robust over disorder [Fig. 6(b) in Appendix C]. As a result, this novel calibration method for the signal is guaranteed by the topological protection of the edge mode, originating from the collective nature of the topological

plasmon polariton, which cannot be observed in nontopological chains or near a single microsphere. This device is therefore more practically sound than a single microsphere or other nontopological microstructures.

The present proposal is within the reach of current experimental technologies. Since the band gap is comparable to the linewidth of modes, the LDOS within the band gap of a nontopological chain is not strictly zero but substantial, which arises from bulk modes. However, this is still an enhancement to LDOS for the topological chain when compared to the nontopological chain, due to the existence of TPP, as indicated by the results in Fig. 4. Therefore, the effect of small linewidth is not that severe. If the experimental procedure is conducted using a narrowband THz gas laser [64,86] or THz quantum cascade laser (QCL) [33], which can resolve this small band gap, or broadband terahertz radiation sources combined with Fourier transform interferometers, it is possible to detect this difference [40,63–69,80,87]. On the other hand, we can incorporate gain media to the microsphere chains to compensate the intrinsic loss of the InSb material and obtain more pronounced distinctions between the LDOS spectra of topological and nontopological chains. Using gain to compensate losses in plasmonic materials in optical spectrum has been extensively investigated by applying optically pumped laser dyes, semiconductors, or quantum dots [88–93] to amplify light intensity [94] and generate lasers in optical spectrum [95,96]. Gain in THz wavelengths can be achieved by using quantum dots or quantum cascade materials like AlGaAs/GaAs and InGaAs/InAlAs systems [97–100] as well as optically pumped graphene [34,101]. Additionally, we can expect if the microspheres are arranged in more sophisticated lattices, such as the honeycomb [61], breathing kagome [102], or bichromatic lattices [103], unidirectionally propagating or more confined TPPs can be realized, which can lead to more pronounced signatures for experimental measurement and thus better sensing performance.

V. CONCLUSION

To summarize, we theoretically investigate the application of TPPs to achieving temperature sensing. We show that TPPs can be realized in a one-dimensional intrinsic InSb microsphere chain. By utilizing the temperature dependence of the permittivity of InSb, the resonance frequency of the TPPs can be thermally tuned. Moreover, the temperature susceptibility of the TPPs can be as high as 0.0264 THz/K at room temperature, leading to a FoM over 150. By calculating the LDOS near the chain as an experimentally detectable signal, we further demonstrate that these TPPs can achieve a strong confinement of radiation near the edges in the band gap and are immune to disorder. We also propose a robust and practical calibration method to correctly obtain the peak frequency of the LDOS spectrum due to TPPs and then the temperature susceptibility, which is based on the ratio between the LDOS of a topological chain and that of a nontopological one. The peak frequency of this ratio is also demonstrated to be immune to disorder. We envisage these TPPs, as well as TPPs in more sophisticated microstructures using the same material, can be utilized as promising candidates for robust and enhanced temperature sensing, especially for on-chip thermometry [104].

ACKNOWLEDGMENTS

This work is supported by the National Natural Science Foundation of China (Grants No. 51906144 and No. 51636004), Science and Technology Commission of Shanghai Municipality (Grant No. 18JC1413300), China Postdoctoral Science Foundation (Grants No. BX20180187 and No. 2019M651493), and the Foundation for Innovative Research Groups of the National Natural Science Foundation of China (Grant No. 51521004).

APPENDIX A: CALCULATION OF BAND STRUCTURES

By applying the Bloch theorem in Eq. (4) for an infinitely long, periodic chain with zero incident field, we can analytically solve the longitudinal Bloch eigenmode with a momentum k_x along the x -axis. Such an eigenmode, in which the dipole moment of i th microsphere can be expressed as $p_{m_i, k_x}(\omega) \exp(ik_x x_i)$ with $m_i = A, B$ according to the sublattice that the i -NP belongs to, should satisfy

$$\frac{\omega^2}{c^2} \sum_{i=1, i \neq j}^N G_{0,xx}(\omega, \mathbf{r}_j, \mathbf{r}_i) p_{m_i, k_x}(\omega) \exp(ik_x x_i) = \alpha^{-1}(\omega) p_{m_j, k_x}(\omega) \exp(ik_x x_j), \quad (\text{A1})$$

where the xx -component of the Green's function is used:

$$G_{0,xx}(x) = -2 \left[\frac{i}{k|x|} - \frac{1}{(k|x|)^2} \right] \frac{\exp(ik|x|)}{4\pi|x|}. \quad (\text{A2})$$

By explicitly carrying out the summations, this equation is equivalently expressed as

$$\frac{\omega^3}{c^3} \begin{pmatrix} a_{11}^L(k_x) & a_{12}^L(k_x) \\ a_{21}^L(k_x) & a_{22}^L(k_x) \end{pmatrix} \begin{pmatrix} p_{A, k_x} \\ p_{B, k_x} \end{pmatrix} = \alpha^{-1}(\omega) \begin{pmatrix} p_{A, k_x} \\ p_{B, k_x} \end{pmatrix}, \quad (\text{A3})$$

where the superscript L indicates the longitudinal modes. Hence we arrive at an eigenvalue problem whose solution corresponds to the dispersion relation (or band structure) of the longitudinal eigenmodes, and the matrix in the left-hand side (LHS) can be regarded as the effective Hamiltonian $H(k_x)$ in the reciprocal space. For a fixed k_x , $\alpha^{-1}(\omega)$ is the eigenvalue of that matrix. This fact allows us to straightforwardly calculate the eigenfrequency and thus the band structure. The diagonal elements in the effective Hamiltonian are given by [41]

$$a_{11}^L(k_x) = a_{22}^L(k_x) = -i \frac{\text{Li}_2(z^+) + \text{Li}_2(z^-)}{2\pi k^2 d^2} + \frac{\text{Li}_3(z^+) + \text{Li}_3(z^-)}{2\pi k^3 d^3}, \quad (\text{A4})$$

where $z^+ = \exp[i(k + k_x)d]$ and $z^- = \exp[i(k - k_x)d]$, and $\text{Li}_s(z) = \sum_{n=1}^{\infty} z^n/n^s$ stands for the polylogarithm (or Jonquière's function) [105]. The off-diagonal series sums as [41]

$$a_{12}^L(k_x) = \left[-i \frac{\Phi(z^+, 2, \beta)}{2\pi k^2 d^2} + \frac{\Phi(z^+, 3, \beta)}{2\pi k^3 d^3} \right] \exp(ik\beta d) + \left[-i \frac{\Phi(z^-, 2, 1-\beta)}{2\pi k^2 d^2} + \frac{\Phi(z^-, 3, 1-\beta)}{2\pi k^3 d^3} \right] \times z^- \exp(-ik\beta d), \quad (\text{A5})$$

and

$$a_{21}^L(k_x) = \left[-i \frac{\Phi(z^+, 2, 1 - \beta)}{2\pi k^2 d^2} + \frac{\Phi(z^+, 3, 1 - \beta)}{2\pi k^3 d^3} \right] \times z^+ \exp(-ik\beta d) + \left[-i \frac{\Phi(z^-, 2, \beta)}{2\pi k^2 d^2} + \frac{\Phi(z^-, 3, \beta)}{2\pi k^3 d^3} \right] \times \exp(ik\beta d), \quad (\text{A6})$$

where $\Phi(z, s, a) = \sum_{n=0}^{\infty} z^n / (n+a)^s$ denotes the Lerch transcendent [105].

Note the above matrix elements are not unique, depending on the choice of unit cell [4], which are chosen such that it fulfills $a_{ij}^L(k_x) = a_{ij}^L(k_x + 2\pi/d)$, i.e., using the periodic gauge [2, 15]. This gauge leads to a \mathbb{Z}_2 invariant in calculating the topological invariant, namely, the complex Zak phase, as will be shown later in Appendix B.

APPENDIX B: CALCULATION OF THE COMPLEX ZAK PHASE

For non-Hermitian systems without exceptional points (EPs), it was recently shown that the complex Zak phase, which is defined by simultaneously using the left-eigenvectors and right-eigenvectors of the non-Hermitian Hamiltonian [13, 106, 107], can be exploited to characterize the band topology of 1D systems. According to Eq. (6), since $a_{12}(k_x)a_{21}(k_x)$ is always not exactly zero when $\beta \neq 0.5$, the bulk band structures are always separable in the complex frequency plane [41, 42, 108], without any EPs. For a separable band structure, it is hence expected that the complex Zak phase is quantized and can describe the topological phase transition [53].

It seems that the present non-Hermitian Hamiltonian exhibits a breaking of chiral symmetry (or sublattice symmetry) due to the existence of diagonal elements $a_{11}(k_x)$ and $a_{22}(k_x)$. According to the conventional Altland-Zirnbauer (AZ) classification [109], this system belongs to the AI class and is topologically trivial [109, 110]. However, a close scrutiny of the effective Hamiltonian tells us that although the frequencies of eigenstates are affected by the diagonal terms (chiral-symmetry breaking terms), the eigenvectors of eigenstates are still the same as those of the chirally symmetric counterpart of the Hamiltonian, i.e.,

$$\tilde{H}(k_x) = \begin{pmatrix} 0 & a_{12}^L(k_x) \\ a_{21}^L(k_x) & 0 \end{pmatrix}, \quad (\text{B1})$$

which obviously fulfills the chiral symmetry condition $\sigma_z \tilde{H}(k_x) \sigma_z = -\tilde{H}(k_x)$. Here σ_i with $i = x, y, z$ refers to Pauli matrices. Such a property can be viewed as a trivial chiral-symmetry breaking as pointed out by Pocock *et al.* [17]. In that sense, the complex Zak phase preserves the feature in a chirally symmetric system, and thus is still quantized and can be used to determine the topology of bulk bandstructure, as recently discussed by Lieu [53]. Note this quantization does not refer to the inversion symmetry, unlike the real Zak phase, which is defined solely based on right eigenvectors and requires the inversion symmetry to be quantized [53]. Nevertheless, here the effective Hamiltonian still obeys this symmetry, i.e., $\sigma_x H(k_x) \sigma_x = H(-k_x)$ over the center of the lattice.

In particular, the normalized (i.e., $\langle p_{k_x}^L | p_{k_x}^R \rangle = 1$) left and right eigenvectors for longitudinal eigenmodes are solved as follows:

$$|p_{k_x}^L\rangle = \begin{pmatrix} p_{A,k_x}^L \\ p_{B,k_x}^L \end{pmatrix} = \frac{1}{\sqrt{2}} \begin{pmatrix} \mp \frac{\sqrt{a_{21}^*(k_x)}}{\sqrt{a_{12}^*(k_x)}} \\ 1 \end{pmatrix}, \quad (\text{B2})$$

$$|p_{k_x}^R\rangle = \begin{pmatrix} p_{A,k_x}^R \\ p_{B,k_x}^R \end{pmatrix} = \frac{1}{\sqrt{2}} \begin{pmatrix} \mp \frac{\sqrt{a_{12}^L(k_x)}}{\sqrt{a_{21}^L(k_x)}} \\ 1 \end{pmatrix}. \quad (\text{B3})$$

The left eigenvector is solved through the relation of $H^\dagger(k_x)|p_{k_x}^L\rangle = E_{k_x}^*|p_{k_x}^L\rangle$. Based on the orthogonality of left and right eigenmodes (namely, biorthogonality) [108, 111, 112] in 1D non-Hermitian systems, the complex Zak phase, as the geometric phase picked up by an eigenmode when it adiabatically evolves across the first Brillouin zone, is expressed as

$$\theta_Z = \int_{\text{BZ}} dk_x \mathcal{A}(k_x) = i \int_{-\pi/d}^{\pi/d} \left[p_{A,k_x}^{L,*} \frac{\partial p_{A,k_x}^R}{\partial k_x} + p_{B,k_x}^{L,*} \frac{\partial p_{B,k_x}^R}{\partial k_x} \right] dk_x = \frac{\arg[a_{21}(k_x)] - \arg[a_{12}(k_x)] + i \ln \left(\frac{|a_{12}(k_x)|}{|a_{21}(k_x)|} \right)}{4} \Big|_{-\pi/d}^{\pi/d}, \quad (\text{B4})$$

where $\mathcal{A}(k_x)$ is the Berry connection. According to this equation, the real part of θ_Z is simply half the difference of the winding numbers of $a_{21}(k_x)$ and $a_{12}(k_x)$ encircling the origin multiplied by π . Since $|a_{12}(-\pi/d)| = |a_{21}(-\pi/d)| = |a_{12}(\pi/d)| = |a_{21}(\pi/d)|$ from Eqs. (A5) and (A6), the imaginary part of θ_Z is exactly zero, as we have already shown in Ref. [41]. Therefore, the complex Zak phase is actually a real quantity [41]. Note the directions of the encircling of $a_{12}(k_x)$ and $a_{21}(k_x)$ are always opposite because $a_{12}(k_x) = a_{21}(-k_x)$. Therefore the winding numbers of $a_{12}(k_x)$ and $a_{21}(k_x)$ are $+1$ and -1 , respectively when the dimerization parameter fulfills $\beta > 0.7$, and are both zero when the dimerization parameter fulfills $\beta < 0.5$. As a consequence, the complex Zak phase for $\beta > 0.5$ and is 0 for $\beta < 0.5$.

Note the above conclusions are made on the basis of the periodic gauge, which is necessary for the quantization of the complex Zak phase [15, 17, 112]. Otherwise if we choose a different unit cell, for instance taking the center of A-type microspheres as the boundary of the unit cell, we would get new matrix elements as $a'_{12} = a_{12} \exp(-ik_x \beta d)$ and $a'_{21} = a_{21} \exp(ik_x \beta d)$, which do not fulfill the periodic gauge. In this circumstance, the complex Zak phase becomes $\theta_Z = (1 + \beta)\pi$ for $\beta > 0.5$ and $\beta\pi$ for $\beta < 0.5$, which is hence not quantized, although we can see that their difference is quantized.

Regarding the BBC, it should be noted our system is very simple with negligible non-Hermiticity (as can be seen from the phase rigidity [41]), which leads to the validity of BBC. As a matter of fact, in our system both time-reversal symmetry and inversion symmetry hold, leading to the absence of any real/imaginary magnetic flux in the viewpoint of non-Hermitian Aharonov-Bohm effect that invalidates the BBC. According to the authors of Ref. [112] who investigated the role of non-Hermiticity in a general non-Hermitian SSH

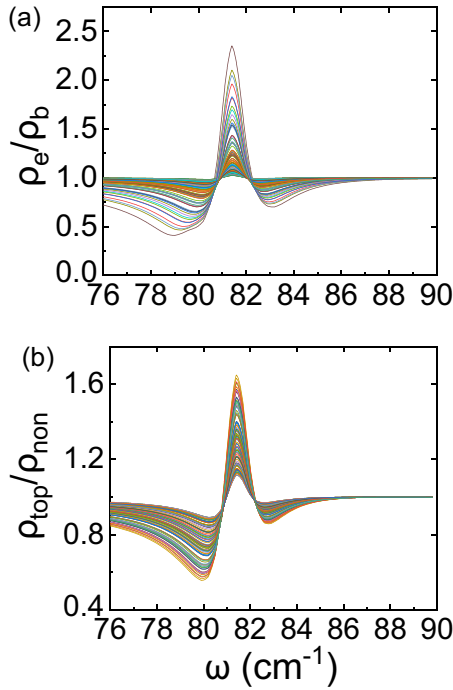


FIG. 6. Calculated LDOS ratios under different disordered configurations. (a) The ratio of the LDOS spectrum near the edge and that near the bulk of a topological chain ρ_e/ρ_b . (b) The ratio of the LDOS spectrum of a topological chain to that of a nontopological chain ρ_{top}/ρ_{non} . The working temperature is $T = 300$ K and the degree of disorder is $\eta = 0.3$, with 100 randomly chosen disordered configurations presented.

model, in our system, BBC holds with the non-Hermiticity being not essential. In addition, we note the arguments in Ref. [112] were based on nearest-neighbor hoppings. Although we included long-range hoppings in our model, they are indeed very weak for longitudinal modes, making the contribution of nearest-neighbor hoppings dominant. In this sense, the band topology and the emergence of edge states are independent of the boundary condition, unlike the case of transverse modes in lattices when the lattice period is

comparable to the wavelength, as we investigated in a previous work [42].

APPENDIX C: CALCULATION OF LDOS

The LDOS can be obtained under the framework of the coupled-dipole equations, while the incident field is replaced by that emitted from a point source [113,114]:

$$\mathbf{p}_j(\omega) = \frac{\omega^2 \alpha(\omega)}{c^2} \left[\mathbf{G}_0(\omega, \mathbf{r}_j, \mathbf{r}_s) \mathbf{p}_s + \sum_{i=1, i \neq j}^N \mathbf{G}_0(\omega, \mathbf{r}_j, \mathbf{r}_i) \mathbf{p}_i(\omega) \right], \quad (\text{C1})$$

where \mathbf{p}_s is the dipole moment of the emitting point source whose position is \mathbf{r}_s . After calculating the electromagnetic responses of all microspheres based on Eq. (C1), the total scattered field of the NP chain at an arbitrary position outside the microspheres is computed as [113,114]

$$\mathbf{E}_s(\mathbf{r}) = \frac{\omega^2}{c^2} \sum_{i=1}^N \mathbf{G}_0(\omega, \mathbf{r}, \mathbf{r}_i) \mathbf{p}_i(\omega). \quad (\text{C2})$$

From the scattered field, it is straightforward to obtain the full Green's function with respect to the point source at \mathbf{r}_s as $\mathbf{G}(\omega, \mathbf{r}, \mathbf{r}_s) = \mathbf{G}_0(\omega, \mathbf{r}, \mathbf{r}_s) + \mathbf{S}(\omega, \mathbf{r}, \mathbf{r}_s)$ [113,114]. Here the elements in scattering field tensor $\mathbf{S}(\omega, \mathbf{r}, \mathbf{r}_s)$ can be calculated through the relation $\mathbf{E}_s(\mathbf{r}) = \mathbf{S}(\omega, \mathbf{r}, \mathbf{r}_s) \mathbf{p}_s$, by aligning the dipole moment of the point source along different axes. Afterwards LDOS is obtained from the full Green's function as

$$\rho(\mathbf{r}_s, \omega) = \frac{2\omega}{\pi c^2} \text{Im}[\text{Tr} \mathbf{G}(\omega, \mathbf{r}_s, \mathbf{r}_s)]. \quad (\text{C3})$$

This total LDOS contains all electromagnetic eigenmodes including both longitudinal and transverse ones.

Figure 6 shows the spectra of the LDOS ratios, ρ_e/ρ_b and ρ_{top}/ρ_{non} , of 100 randomly chosen disordered configurations. It can be seen that the peak frequencies of these ratios are quite robust under disorder.

[1] M. Z. Hasan and C. L. Kane, *Rev. Mod. Phys.* **82**, 3045 (2010).
 [2] T. Ozawa, H. M. Price, A. Amo, N. Goldman, M. Hafezi, L. Lu, M. C. Rechtsman, D. Schuster, J. Simon, O. Zilberberg, and I. Carusotto, *Rev. Mod. Phys.* **91**, 015006 (2019).
 [3] C. He, X. Ni, H. Ge, X.-C. Sun, Y.-B. Chen, M.-H. Lu, X.-P. Liu, and Y.-F. Chen, *Nat. Phys.* **12**, 1124 (2016).
 [4] M. Atala, M. Aidelsburger, J. T. Barreiro, D. Abanin, T. Kitagawa, E. Demler, and I. Bloch, *Nat. Phys.* **9**, 795 (2013).
 [5] R. Süsstrunk and S. D. Huber, *Science* **349**, 47 (2015).
 [6] L. Lu, J. D. Joannopoulos, and M. Soljačić, *Nat. Photon.* **8**, 821 (2014).
 [7] A. B. Khanikaev and G. Shvets, *Nat. Photon.* **11**, 763 (2017).

[8] M. S. Rider, S. J. Palmer, S. R. Pockock, X. Xiao, P. Arroyo Huidobro, and V. Giannini, *J. Appl. Phys.* **125**, 120901 (2019).
 [9] B.-Y. Xie, H.-F. Wang, X.-Y. Zhu, M.-H. Lu, Z. D. Wang, and Y.-F. Chen, *Opt. Express* **26**, 24531 (2018).
 [10] C. Poli, M. Bellec, U. Kuhl, F. Mortessagne, and H. Schomerus, *Nat. Commun.* **6**, 6710 (2015).
 [11] R. El-Ganainy and M. Levy, *Opt. Lett.* **40**, 5275 (2015).
 [12] P. St.-Jean, V. Goblots, E. Galopin, A. Lemaître, T. Ozawa, L. Le Gratiet, I. Sagnes, J. Bloch, and A. Amo, *Nat. Photon.* **11**, 651 (2017).
 [13] M. Parto, S. Wittek, H. Hodaei, G. Harari, M. A. Bandres, J. Ren, M. C. Rechtsman, M. Segev, D. N. Christodoulides, and M. Khajavikhan, *Phys. Rev. Lett.* **120**, 113901 (2018).

- [14] H. Zhao, P. Miao, M. H. Teimourpour, S. Malzard, R. El-Ganainy, H. Schomerus, and L. Feng, *Nat. Commun.* **9**, 981 (2018).
- [15] C. W. Ling, M. Xiao, C. T. Chan, S. F. Yu, and K. H. Fung, *Opt. Express* **23**, 2021 (2015).
- [16] C. A. Downing and G. Weick, *Phys. Rev. B* **95**, 125426 (2017).
- [17] S. Pocock, X. Xiao, P. A. Huidobro, and V. Giannini, *ACS Photon.* **5**, 2271 (2018).
- [18] C. A. Downing and G. Weick, *Eur. Phys. J. B* **91**, 253 (2018).
- [19] S. R. Pocock, P. A. Huidobro, and G. Vincenzo, *Nanophotonics* **8**, 1337 (2019).
- [20] B. X. Wang and C. Y. Zhao, *J. Appl. Phys.* **127**, 073106 (2020).
- [21] C. Xu, P. Zhang, D. Zhao, H. Guo, M. Huang, and S. Ke, *Appl. Sci.* **9**, 4152 (2019).
- [22] J. W. You, Z. Lan, and N. C. Panoiu, *Sci. Adv.* **6**, eaaz3910 (2020).
- [23] J. Wiersig, *Phys. Rev. Lett.* **112**, 203901 (2014).
- [24] L. Feng, R. El-Ganainy, and L. Ge, *Nat. Photon.* **11**, 752 (2017).
- [25] W. Chen, S. Kaya Özdemir, G. Zhao, J. Wiersig, and L. Yang, *Nature* **548**, 192 (2017).
- [26] R. El-Ganainy, K. G. Makris, M. Khajavikhan, Z. H. Musslimani, S. Rotter, and D. N. Christodoulides, *Nat. Phys.* **14**, 11 (2018).
- [27] L. Jin, H. C. Wu, B.-B. Wei, and Z. Song, *Phys. Rev. B* **101**, 045130 (2020).
- [28] S. M. Zhang, X. Z. Zhang, L. Jin, and Z. Song, *Phys. Rev. A* **101**, 033820 (2020).
- [29] W. P. Su, J. R. Schrieffer, and A. J. Heeger, *Phys. Rev. Lett.* **42**, 1698 (1979).
- [30] P. Halevi and F. Ramos-Mendieta, *Phys. Rev. Lett.* **85**, 1875 (2000).
- [31] J. Gómez Rivas, J. A. Sánchez-Gil, M. Kuttge, P. Haring Bolívar, and H. Kurz, *Phys. Rev. B* **74**, 245324 (2006).
- [32] T. Taliercio and P. Biagioni, *Nanophotonics* **8**, 949 (2019).
- [33] B. S. Williams, *Nat. Photon.* **1**, 517 (2007).
- [34] P. Weis, J. L. Garcia-Pomar, and M. Rahm, *Opt. Express* **22**, 8473 (2014).
- [35] D. Spirito, D. Coquillat, S. L. De Bonis, A. Lombardo, M. Bruna, A. C. Ferrari, V. Pellegrini, A. Tredicucci, W. Knap, and M. S. Vitiello, *Appl. Phys. Lett.* **104**, 061111 (2014).
- [36] H. Matsumoto, I. Watanabe, A. Kasamatsu, and Y. Monnai, *Nat. Electron.* **3**, 122 (2020).
- [37] H. Zhao, B. Quan, X. Wang, C. Gu, J. Li, and Y. Zhang, *ACS Photon.* **5**, 1726 (2018).
- [38] X. Yang, X. Zhao, K. Yang, Y. Liu, Y. Liu, W. Fu, and Y. Luo, *Trends Biotechnol.* **34**, 810 (2016).
- [39] T. L. Cocker, V. Jelic, M. Gupta, S. J. Molesky, J. A. Burgess, G. De Los Reyes, L. V. Titova, Y. Y. Tsui, M. R. Freeman, and F. A. Hegmann, *Nat. Photon.* **7**, 620 (2013).
- [40] N. A. Aghamiri, F. Huth, A. J. Huber, A. Fali, R. Hillenbrand, and Y. Abate, *Opt. Express* **27**, 24231 (2019).
- [41] B. X. Wang and C. Y. Zhao, *Phys. Rev. A* **98**, 023808 (2018).
- [42] B. X. Wang and C. Y. Zhao, *Phys. Rev. B* **98**, 165435 (2018).
- [43] E. Tervo, Z. Zhang, and B. Cola, *Phys. Rev. Mater.* **1**, 015201 (2017).
- [44] V. A. Markel and A. K. Sarychev, *Phys. Rev. B* **75**, 085426 (2007).
- [45] S. Y. Park and D. Stroud, *Phys. Rev. B* **69**, 125418 (2004).
- [46] R. W. Cunningham and J. B. Gruber, *J. Appl. Phys.* **41**, 1804 (1970).
- [47] J. Han and A. Lakhtakia, *J. Mod. Opt.* **56**, 554 (2009).
- [48] S. C. Howells and L. A. Schlie, *Appl. Phys. Lett.* **69**, 550 (1996).
- [49] C. Kittel, *Introduction to Solid State Physics* (Wiley, New York, 2004).
- [50] M. Oszwaldowski and M. Zimpel, *J. Phys. Chem. Solids* **49**, 1179 (1988).
- [51] N. Cherroret, D. Delande, and B. A. van Tiggelen, *Phys. Rev. A* **94**, 012702 (2016).
- [52] W. H. Weber and G. W. Ford, *Phys. Rev. B* **70**, 125429 (2004).
- [53] S. Lieu, *Phys. Rev. B* **97**, 045106 (2018).
- [54] R. Wang, M. Röntgen, C. V. Morfonios, F. A. Pinheiro, P. Schmelcher, and L. D. Negro, *Opt. Lett.* **43**, 1986 (2018).
- [55] Z. Fei, A. Rodin, G. O. Andreev, W. Bao, A. McLeod, M. Wagner, L. Zhang, Z. Zhao, M. Thiemens, G. Dominguez, M. M. Fogler, A. H. Castro Neto, C. N. Lau, F. Keilmann, and D. N. Basov, *Nature (London)* **487**, 82 (2012).
- [56] N. Wang, G.-Q. Liu, W.-H. Leong, H. Zeng, X. Feng, S.-H. Li, F. Dolde, H. Fedder, J. Wrachtrup, X.-D. Cui, S. Yang, Q. Li, and R.-B. Liu, *Phys. Rev. X* **8**, 011042 (2018).
- [57] C. Chen, L. Jin, and R.-B. Liu, *New J. Phys.* **21**, 083002 (2019).
- [58] Y. Ma, N. Nguyen-Huu, J. Zhou, H. Maeda, Q. Wu, M. Eldlio, J. Pištora, and M. Cada, *IEEE J. Sel. Top. Quantum Electron.* **23**, 4601607 (2017).
- [59] S. Kruk, A. Slobozhanyuk, D. Denkova, A. Poddubny, I. Kravchenko, A. Miroshnichenko, D. Neshev, and Y. Kivshar, *Small* **13**, 1603190 (2017).
- [60] A. Slobozhanyuk, A. V. Shchelokova, X. Ni, S. Hossein Mousavi, D. A. Smirnova, P. A. Belov, A. Alù, Y. S. Kivshar, and A. B. Khanikaev, *Appl. Phys. Lett.* **114**, 031103 (2019).
- [61] M. Proctor, R. V. Craster, S. A. Maier, V. Giannini, and P. A. Huidobro, *ACS Photon.* **6**, 2985 (2019).
- [62] S. Peng, N. J. Schilder, X. Ni, J. van de Groep, M. L. Brongersma, A. Alù, A. B. Khanikaev, H. A. Atwater, and A. Polman, *Phys. Rev. Lett.* **122**, 117401 (2019).
- [63] H.-T. Chen, R. Kersting, and G. C. Cho, *Appl. Phys. Lett.* **83**, 3009 (2003).
- [64] A. J. Huber, F. Keilmann, J. Wittborn, J. Aizpurua, and R. Hillenbrand, *Nano Lett.* **8**, 3766 (2008).
- [65] M. Wächter, M. Nagel, and H. Kurz, *Appl. Phys. Lett.* **95**, 041112 (2009).
- [66] K. Moon, Y. Do, M. Lim, G. Lee, H. Kang, K.-S. Park, and H. Han, *Appl. Phys. Lett.* **101**, 011109 (2012).
- [67] K. Moon, H. Park, J. Kim, Y. Do, S. Lee, G. Lee, H. Kang, and H. Han, *Nano Lett.* **15**, 549 (2015).
- [68] F. Kuszewski, H.-G. von Ribbeck, J. Döring, S. Winnerl, L. M. Eng, and S. C. Kehr, *Appl. Phys. Lett.* **108**, 113102 (2016).
- [69] C. Maissen, S. Chen, E. Nikulina, A. Govyadinov, and R. Hillenbrand, *ACS Photon.* **6**, 1279 (2019).
- [70] K. Joulain, R. Carminati, J.-P. Mulet, and J.-J. Greffet, *Phys. Rev. B* **68**, 245405 (2003).
- [71] J. Chen, M. Badioli, P. Alonso-González, S. Thongrattanasiri, F. Huth, J. Osmond, M. Spasenović, A. Centeno, A. Pesquera, P. Godignon, A. Zurutuza Elorza, N. Camara, F. Javier García de Abajo, R. Hillenbrand, and F. H. L. Koppens, *Nature (London)* **487**, 77 (2012).

- [72] É. Castanié, R. Vincent, R. Pierrat, and R. Carminati, *Int. J. Opt.* **2012**, 452047 (2012).
- [73] A. S. McLeod, P. Kelly, M. D. Goldflam, Z. Gainsforth, A. J. Westphal, G. Dominguez, M. H. Thiemens, M. M. Fogler, and D. N. Basov, *Phys. Rev. B* **90**, 085136 (2014).
- [74] R. Carminati, A. Cazé, D. Cao, F. Peragut, V. Krachmalnicoff, R. Pierrat, and Y. D. Wilde, *Surf. Sci. Rep.* **70**, 1 (2015).
- [75] K.-T. Lin, S. Komiyama, and Y. Kajihara, *Opt. Lett.* **41**, 484 (2016).
- [76] L. Xiong, C. Forsythe, M. Jung, A. McLeod, S. Sunku, Y. Shao, G. Ni, A. Sternbach, S. Liu, J. Edgar, E. J. Mele, M. M. Fogler, G. Shvets, C. R. Dean, and D. N. Basov, *Nat. Commun.* **10**, 4780 (2019).
- [77] R. Prasad and R. Vincent, *Phys. Rev. B* **94**, 165440 (2016).
- [78] Y. Huang, D. Legrand, R. Vincent, E. A. Dogbe Foli, D. Nowak, G. Lerondel, R. Bachelot, T. Taliercio, F. Barho, L. Cerutti, F. Gonzalez-Posada, B. K. Tay, and A. Bruyant, *ACS Photon.* **5**, 4352 (2018).
- [79] H.-W. Wu, Y. Li, H.-J. Chen, Z.-Q. Sheng, H. Jing, R.-H. Fan, and R.-W. Peng, *ACS Appl. Nano Mater.* **2**, 1045 (2019).
- [80] H.-G. von Ribbeck, M. Brehm, D. van der Weide, S. Winnerl, O. Drachenko, M. Helm, and F. Keilmann, *Opt. Express* **16**, 3430 (2008).
- [81] V. Trukhin, A. V. Andrianov, V. Bykov, A. Golubok, N. N. Zinov'ev, L. Samoilov, I. Sapozhnikov, A. Trukhin, and M. Fel'shtyn, *JETP Lett.* **93**, 119 (2011).
- [82] R. Hillenbrand, T. Taubner, and F. Keilmann, *Nature (London)* **418**, 159 (2002).
- [83] A. Cvitkovic, N. Ocelic, and R. Hillenbrand, *Opt. Express* **15**, 8550 (2007).
- [84] H. T. Stinson, J. S. Wu, B. Y. Jiang, Z. Fei, A. S. Rodin, B. C. Chapler, A. S. McLeod, A. Castro Neto, Y. S. Lee, M. M. Fogler, and D. N. Basov, *Phys. Rev. B* **90**, 014502 (2014).
- [85] O. Khatib, H. A. Bechtel, M. C. Martin, M. B. Raschke, and G. L. Carr, *ACS Photon.* **5**, 2773 (2018).
- [86] P. Chevalier, A. Amirzhan, F. Wang, M. Piccardo, S. G. Johnson, F. Capasso, and H. O. Everitt, *Science* **366**, 856 (2019).
- [87] Y. Jiang, M. Liang, B. Jin, L. Kang, W. Xu, J. Chen, and P. Wu, *Chin. Sci. Bull.* **57**, 573 (2012).
- [88] S. A. Ramakrishna and J. B. Pendry, *Phys. Rev. B* **67**, 201101(R) (2003).
- [89] S. Wuestner, A. Pusch, K. L. Tsakmakidis, J. M. Hamm, and O. Hess, *Phys. Rev. Lett.* **105**, 127401 (2010).
- [90] J. Yang, C. Sauvan, H. T. Liu, and P. Lalanne, *Phys. Rev. Lett.* **107**, 043903 (2011).
- [91] A. Veltri and A. Aradian, *Phys. Rev. B* **85**, 115429 (2012).
- [92] Y. J. Zhou, Q. Y. Li, H. Z. Zhao, and T. J. Cui, *Adv. Mater. Technol.* **5**, 1900767 (2020), <https://onlinelibrary.wiley.com>.
- [93] S. Xiao, V. P. Drachev, A. V. Kildishev, X. Ni, U. K. Chettiar, H.-K. Yuan, and V. M. Shalae, *Nature (London)* **466**, 735 (2010).
- [94] J. M. Hamm, S. Wuestner, K. L. Tsakmakidis, and O. Hess, *Phys. Rev. Lett.* **107**, 167405 (2011).
- [95] R. F. Oulton, V. J. Sorger, T. Zentgraf, R.-M. Ma, C. Gladden, L. Dai, G. Bartal, and X. Zhang, *Nature (London)* **461**, 629 (2009).
- [96] O. Hess, J. B. Pendry, S. A. Maier, R. F. Oulton, J. M. Hamm, and K. L. Tsakmakidis, *Nat. Mater.* **11**, 573 (2012).
- [97] R. Köhler, A. Tredicucci, F. Beltram, H. E. Beere, E. H. Linfield, A. G. Davies, D. A. Ritchie, R. C. Iotti, and F. Rossi, *Nature (London)* **417**, 156 (2002).
- [98] L. Ajili, G. Scalari, N. Hoyler, M. Giovannini, and J. Faist, *Appl. Phys. Lett.* **87**, 141107 (2005).
- [99] R. W. Adams, K. Vijayraghavan, Q. J. Wang, J. Fan, F. Capasso, S. P. Khanna, A. G. Davies, E. H. Linfield, and M. A. Belkin, *Appl. Phys. Lett.* **97**, 131111 (2010).
- [100] B. A. Burnett and B. S. Williams, *Opt. Express* **24**, 25471 (2016).
- [101] S. Boubanga-Tombet, S. Chan, T. Watanabe, A. Satou, V. Ryzhii, and T. Otsuji, *Phys. Rev. B* **85**, 035443 (2012).
- [102] A. El Hassan, F. K. Kunst, A. Moritz, G. Andler, E. J. Bergholtz, and M. Bourennane, *Nat. Photon.* **13**, 697 (2019).
- [103] F. Alpeggiani and L. Kuipers, *Optica* **6**, 96 (2019).
- [104] C. T. Nguyen, R. E. Evans, A. Sipahigil, M. K. Bhaskar, D. D. Sukachev, V. N. Agafonov, V. A. Davydov, L. F. Kulikova, F. Jelezko, and M. D. Lukin, *Appl. Phys. Lett.* **112**, 203102 (2018).
- [105] F. W. Olver, D. W. Lozier, R. F. Boisvert, and C. W. Clark, *NIST Handbook of Mathematical Functions* (Cambridge University Press, Cambridge, England, 2010).
- [106] F. Dangel, M. Wagner, H. Cartarius, J. Main, and G. Wunner, *Phys. Rev. A* **98**, 013628 (2018).
- [107] E. J. Bergholtz, J. C. Budich, and F. K. Kunst, [arXiv:1912.10048](https://arxiv.org/abs/1912.10048).
- [108] H. Shen, B. Zhen, and L. Fu, *Phys. Rev. Lett.* **120**, 146402 (2018).
- [109] A. P. Schnyder, S. Ryu, A. Furusaki, and A. W. W. Ludwig, *Phys. Rev. B* **78**, 195125 (2008).
- [110] J. K. Asbóth, L. Oroszlány, and A. P. Pályi, *A Short Course on Topological Insulators: Band Structure and Edge States in One and Two Dimensions* (Springer, New York, 2016).
- [111] L. Jin, *Phys. Rev. A* **96**, 032103 (2017).
- [112] L. Jin and Z. Song, *Phys. Rev. B* **99**, 081103(R) (2019).
- [113] R. Pierrat and R. Carminati, *Phys. Rev. A* **81**, 063802 (2010).
- [114] A. Caze, R. Pierrat, and R. Carminati, *Phys. Rev. Lett.* **111**, 053901 (2013).